GEOPHYSICS, VOL. 78, NO. 2 (MARCH-APRIL 2013); P. WA55–WA70, 18 FIGS.
10.1190/GEO2012-0302.1

Wavefield-separation methods for dual-sensor towed-streamer data

Anthony Day[1], Tilman Klüver[1], Walter Söllner[1], Hocine Tabti[1], and David Carlson[2]

ABSTRACT

A dual-sensor towed streamer records the pressure and vertical component of particle motion associated with the incident wavefield that may be used to separate the wavefield into its up- and downgoing parts. This procedure requires information about the water properties (wave-propagation velocity and density) and is robust in the presence of errors in the estimation of these quantities of the magnitude likely to be encountered. In practice, the particle motion data recorded by current towed marine streamers encounter very strong mechanical noise such that, for the lowest frequencies, the wavefield separation must be approximated by deconvolving the ghost function from the pressure data. This procedure requires information about the streamer depth and is robust to small depth errors over the frequency range for which it is required for dual-sensor streamer processing, but it is much more sensitive if applied over the bandwidth necessary to deghost pressure data acquired at a conventional streamer depth. The signal-to-noise ratio can be further enhanced by recombining the up- and downgoing pressure fields at the sea surface, which has the effect of applying a ghostlike filter to noise that is recorded by only one of the two sensors. In practical marine acquisition scenarios, spatial sampling is often insufficient to yield an accurate result, especially in the crossline direction. If each streamer is processed independently assuming that the wavefield propagation is purely inline, significant errors can be introduced. For arrivals with high emergent angles, errors may also be introduced even if the wavefield propagation actually is purely inline due to incorrect treatment of spatially aliased energy. However, these effects are almost entirely confined to very shallow events. They can be mitigated by using independently derived information about the crossline propagation angle and, for data comprising predominantly forward scattered energy, appropriate application of linear moveout.

INTRODUCTION

Traditionally, towed marine seismic acquisition has been conducted using streamers containing pressure sensors to record seismic signals originating from a seismic source comprising arrays of air guns, with the receivers and source deployed at constant depths. The recorded data have sea surface "ghosts," or reflections from the sea surface, at the source and receiver side. In the case in which the sea surface is assumed to behave as a flat free surface, and it is assumed that the signal undergoes no modification on traveling to the sea surface and back again, the recorded pressure signal from the sea-surface ghost is a polarity-reversed time-delayed copy of the recorded primary pressure signal. On the source side, the copy is of the downgoing source energy, and on the receiver side, the copy is of the upgoing primary energy scattered from the subsurface below. The time delay of the ghost results in constructive and destructive interference at frequencies imposed by the source and receiver depths. Figure 1 shows the amplitude spectrum of ideal ghost functions for several example acquisition depths.

In practical marine seismic acquisition, the sea surface may not behave in such a theoretically perfect fashion. Nevertheless, spectral analysis of field data indicates the presence of spectral "notches" with very low signal-to-noise ratio (S/N) at frequencies characteristic of the source and receiver depths. Because the source and receiver depths are usually different from each other, they give rise to two distinct sets of notches. There is essentially no usable information in the vicinity of these spectral notches; hence, any processing-based solution to recover information in these parts of the spectrum must be based on reconstructing the data that have not been recorded from other parts of the data with higher S/N. Because such

Manuscript received by the Editor 1 August 2012; published online 20 March 2013.
[1]Petroleum Geo-Services, Lysaker, Norway. E-mail: anthony.day@pgs.com; tilman.kluver@pgs.com; walter.sollner@pgs.com; hocine.tabti@pgs.com.
[2]Petroleum Geo-Services, Houston, Texas, USA. E-mail: dave.carlson@pgs.com.

a data reconstruction exercise is a challenging undertaking (Ghosh, 2000), the source and receiver depths for towed marine seismic acquisition have typically been chosen such that these spectral notches are outside the usable bandwidth for the particular target of interest. This requirement has inevitably led to compromises in survey design in which there are multiple targets of interest because it is not always possible to design the acquisition such that the recorded bandwidth is optimal for all targets.

In recent years, several towed marine acquisition techniques have been developed that allow the bandwidth limitations of the traditional acquisition approach to be overcome. A common feature of all these methods is that they do not seek to mitigate the presence of ghosts, which are an inevitable product of marine acquisition, but rather they record information with different ghost characteristics such that, when all the data are combined, there is good S/N at a wider range of frequencies. One approach is based on recording data with multiple streamers at different constant depths (e.g., Sønneland, et al., 1986; Amundsen, 1993; Hill et al., 2006; Moldoveanu et al., 2007; Bunting et al., 2011). If the same wavefield is recorded by receivers at two different depths, the receiver-side ghost effects for each depth will be different. Provided the depths are chosen such that there are no common spectral notches within the usable bandwidth, then, wherever there is a spectral notch for one depth, good S/N will be recorded at the other depth, thereby increasing the usable bandwidth compared to a single depth. For the examples in Figure 1, the depth combination that will provide a stable result over the widest range of frequencies is 8 and 20 m because the first common spectral notch for these two depths is at a frequency in excess of 180 Hz. Another approach is to vary the depth of the streamers along their length (e.g., Soubaras and Dowle, 2010). This acquisition geometry results in different ghost characteristics for different channels such that, when they are combined in imaging, there are signal contributions at a wider range of frequencies in the final image than can be achieved using a single streamer depth. A third alternative is to use a dual-sensor streamer that records the seismic wavefield using pressure and vertical particle velocity sensors (e.g., Carlson et al., 2007; Tenghamn et al., 2007).

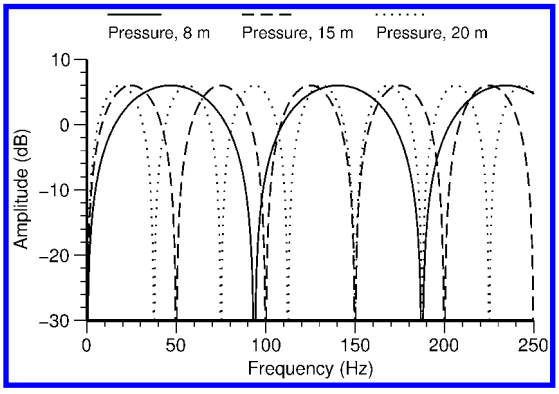

Figure 1. Amplitude spectra of pressure ghost functions for 8-, 15-, and 20-m depths for a water velocity of 1500 m/s and assuming vertical incidence.

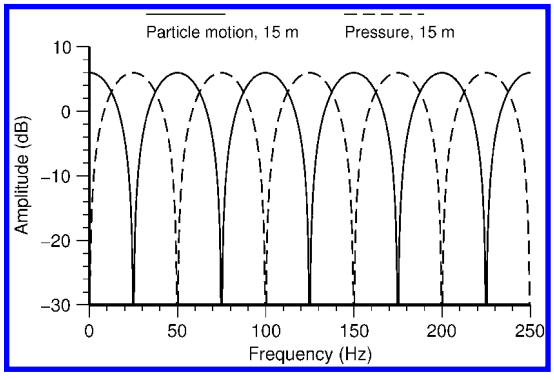

Figure 2. Pressure and particle motion ghost functions at a 15-m depth for a water velocity of 1500 m/s and assuming vertical incidence.

The ghost characteristics of the vertical particle velocity sensor always exactly complement those of the pressure sensor independently of towing depth: Wherever one sensor has a spectral notch, the other sensor records a high S/N, as shown in Figure 2. The polarity of the primary is reversed at the sea surface due to a negative reflection coefficient before being recorded as a ghost reflection on the pressure and particle velocity sensors. The omnidirectional pressure sensor records this polarity reversal, whereas it is counteracted by the directionality of the vertical particle velocity sensor. This results in perfectly complementary frequencies for constructive and destructive interference between the primary and ghost energy on both sensors. This feature has been understood and exploited in ocean bottom acquisition systems for many years (e.g., Schneider and Backus, 1964; Barr and Sanders, 1989) and has also been suggested for towed streamer acquisition (Loewenthal, 1994). However, it is only relatively recently that it has been successfully implemented for towed marine acquisition (Tenghamn et al., 2007). Finally, note that all the methods described here focus on acquisition approaches to mitigating the effect of receiver-side ghosts. However, similar approaches have also been proposed for extending the usable bandwidth emitted by the source (e.g., Ziolkowski, 1971; Egan et al., 2007; Cambois et al., 2009a; Parkes and Hegna, 2011).

In this paper we focus on how the data recorded by a dual-sensor towed streamer are used in practice to increase the usable bandwidth. We focus on relatively simple approaches to processing dual-sensor towed streamer data to illustrate the underlying signal processing issues that must be overcome for realistic acquisition geometries. The same physical principles have been used to develop inversion-based approaches to deghosting and data reconstruction that additionally take advantage of recorded crossline particle motion data (Özbek et al., 2010; Özdemir et al., 2010; Vassallo et al., 2010), but these methods will not be discussed in this paper. We show how the data may be used to separate the recorded wavefield into its up- and downgoing parts, thereby allowing the receiver-side ghost to be distinguished from the upgoing scattered energy. This wavefield-separation method is relatively straightforward, based on fundamental geophysical principles, and it permits great flexibility in how the resulting data can be used in subsequent processing steps. For example, the up- and downgoing wavefields can be combined to predict surface-related multiples, thereby eliminating some of the assumptions commonly made when conventional data are used in this procedure and yielding a superior result (Frijlink et al., 2011; van Borselen et al., 2011). A further example

is combining up- and downgoing wavefields in the imaging step, which allows us to make use of multiple energy in the image. The contribution from the multiple energy in the migration results in better illumination of the subsurface compared to the case in which the multiple energy is discarded (Amundsen et al., 2008; Whitmore et al., 2010; Vasconcelos, 2011; Lameloise et al., 2012). Note that the wavefield-separation procedure described in this paper is commonly applied to raw field data because this is often the most convenient stage to apply the procedure; however, this is not a requirement and the same theoretical basis may be used to perform wavefield separation at another point in the processing sequence. An example of wavefield separation in the imaging step is given by Klüver (2009).

In practice, the data we acquire in the field are often imperfect when measured against the ideal theoretical requirement for noise-free, infinite aperture data. The objective of this paper is to discuss some of the limitations of practical field acquisition, their importance to the accuracy of the final result, and how they can be overcome.

THEORETICAL BACKGROUND

The theory of how dual-sensor data can be used to separate the recorded wavefield into its up- and downgoing parts has been discussed in detail by several authors (e.g., Claerbout, 1976; Fokkema and van den Berg, 1993; Weglein and Secrest, 1990; Amundsen, 1993; Ikelle and Amundsen, 2005). A brief overview of the relevant theory is presented here.

The derivation of the wavefield-separation method for dual-sensor marine data as Fokkema and van den Berg (1993) describe is based on the application of the reciprocity theorem to solve the acoustic-wave equation. Consider a domain in an acoustic medium (such as water) containing no sources and bounded by two arbitrary surfaces of infinite extent as depicted in Figure 3. The bounding surfaces must be defined such that the deepest point of the upper boundary is shallower than the shallowest point on the lower boundary. The reciprocity theorem can be used to define the pressure at a point $\mathbf{x}_0$ inside that domain at a level between the inner extremities of the bounding surfaces in terms of an integral of the pressure and normal derivative of the pressure recorded at the bounding surfaces as follows:

$$p(\mathbf{x}_0,\omega) = \int_{S1+S2} dS\mathbf{n}\cdot[g(\mathbf{x},\omega;\mathbf{x}_0)\nabla p(\mathrm{x},\omega) - p(\mathbf{x},\omega)\nabla g(\mathrm{x},\omega;\mathbf{x}_0)], \quad (1)$$

where p is the pressure wavefield for angular frequency ω, $\mathbf{n}$ is the outward unit normal vector to the bounding surface, and g is the causal Green's function (for a homogeneous background) that describes the propagation of the wavefield from a point $\mathbf{x}$ on the recording surface to $\mathbf{x}_0$. Fokkema and van den Berg (1993) show that, if the contributions from the lower bounding surface S1 are considered in isolation, we obtain from the field reciprocity theorem with a causal Green's function an expression for the upgoing pressure wavefield p^{up}. They also derive a similar expression for the downgoing pressure wavefield p^{down} from the power reciprocity with an anticausal Green's function $\tilde{g}$:

$$\begin{aligned} p^{\mathrm{up}}(\mathbf{x}_0,\omega) &= \int_{S1} dS\mathbf{n}\cdot[g(\mathbf{x},\omega;\mathbf{x}_0)\nabla p(\mathbf{x},\omega) \\ &\quad - p(\mathbf{x},\omega)\nabla g(\mathbf{x},\omega;\mathbf{x}_0)], \\ p^{\mathrm{down}}(\mathbf{x}_0,\omega) &= \int_{S1} dS\mathbf{n}\cdot[-\tilde{g}(\mathbf{x},\omega;\mathbf{x}_0)\nabla p(\mathbf{x},\omega) \\ &\quad - p(\mathbf{x},\omega)\nabla\tilde{g}(\mathbf{x},\omega;\mathbf{x}_0)]. \end{aligned} \quad (2)$$

The dot product of the unit normal vector and the gradient of the pressure field is related to the normal component of the particle velocity vector v_n by the equation of motion,

$$\mathbf{n}\cdot\nabla p = -i\omega\rho v_n, \quad (3)$$

where ρ is the density of the medium in which the wave is propagating — water in this case. From equations 2 and 3, we see that recordings of the pressure and the component of particle velocity normal to the recording surface are sufficient to perform wavefield separation, subject to adequate spatial sampling.

Consider the case in which the recording surface S1 is horizontal at a depth z_r, the desired output locations $\mathbf{x}_0$ all lie on a horizontal surface at depth z_o, the water density ρ at depth z_r is constant, and the propagation velocity in water between depths z_r and z_o is a constant c. When these conditions are satisfied, the expressions in equation 2 reduce to simplified expressions for the up- and downgoing pressure fields as functions of angular frequency and the horizontal angular wavenumbers, k_x and k_y, as follows:

$$\begin{aligned} P^{\mathrm{up}}(k_x,k_y,\omega|z_o) &= \frac{1}{2}\left(P(k_x,k_y,\omega|z_r) - \frac{\omega\rho}{k_z}V_z(k_x,k_y,\omega|z_r)\right) \\ &\quad \exp(-ik_z(z_r-z_o)), \\ P^{\mathrm{down}}(k_x,k_y,\omega|z_o) &= \frac{1}{2}\left(P(k_x,k_y,\omega|z_r) + \frac{\omega\rho}{k_z}V_z(k_x,k_y,\omega|z_r)\right) \\ &\quad \exp(ik_z(z_r-z_o)). \end{aligned} \quad (4)$$

The vertical component of particle velocity, i.e., normal to the recording surface in this special case with the convention that a positive value indicates downward motion, is V_z, and k_z is the magnitude of the vertical angular wavenumber, which can be expressed as

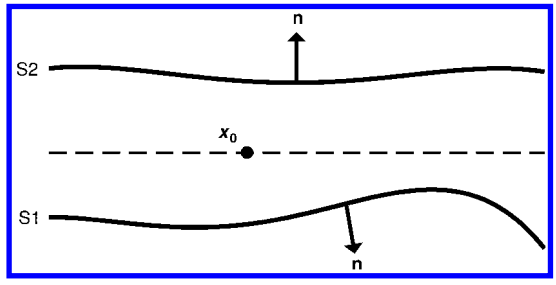

Figure 3. The domain in which the reciprocity theorem is used to derive expressions for wavefield separation. Pressure and the pressure gradient normal to recording surfaces S1 and S2 are used to determine the pressure at a point $\mathbf{x}_0$ that lies on a horizontal surface that crosses neither S1 nor S2. Vector $\mathbf{n}$ denotes the outward pointing normal to surfaces S1 and S2.

$$k_z = \sqrt{\left(\frac{\omega}{c}\right)^2 - k_x^2 - k_y^2}. \quad (5)$$

A dual-sensor streamer records the pressure and the vertical component of particle motion. Depending on the streamer construction, the particle motion sensor might record the normal component of the particle velocity or the normal component of the acceleration, which in the latter case can be integrated with respect to time to obtain particle velocity. Consequently, the two representations of the wavefield that are required to perform wavefield separation are recorded by a dual-sensor streamer. From inspection of the simplified expressions in equations 4 and 5, it can be seen that, if the output datum level is at a very small distance above the recording surface ($z_o \approx z_r$), the only additional information that is required, beyond that recorded by the sensors in the streamer, is the density and propagation velocity in water at the level of the receivers, which is needed for two reasons. First, the constant of proportionality that relates particle velocity to pressure is the acoustic impedance, or the product of density and propagation velocity. This is required because we combine a measurement of pressure and a measurement of particle velocity related to the same wavefield. Second, we record the normal (or vertical) component of particle motion whereas pressure is a scalar quantity. Consequently, an obliquity scaling is required to combine them correctly. This obliquity scaling is represented by the k_z term, which is calculated using the expression in equation 5 from the horizontal wavenumbers and the total magnitude of the angular wavenumber vector, which in turn is related to the angular frequency and the propagation velocity. Water is an acoustic medium whose density and propagation velocity can both be measured directly in the field, and these properties tend to vary slowly and smoothly in space. As a result, it is relatively easy to match the pressure and particle motion signals recorded in a towed streamer without any data-dependent calibration. The latter is often a requirement for ocean bottom recordings in which the receivers are located at a boundary between an acoustic and an elastic medium whose properties are usually less well known and cannot necessarily be assumed to be smoothly varying (e.g., Backus et al., 2007).

To accurately redatum the output of wavefield separation to a different level, information about the propagation velocity is required away from the recording surface. In the simplified case represented by equation 4 in which the propagation velocity is assumed to be constant, this redatuming is a simple phase shift represented by the complex exponential. Note that this complex exponential contains the obliquity term k_z, which indicates a time shift dependent on the emergent angle. In the general case represented by equation 2, the propagation from the recording surface to the desired output location is described by the Green's functions, which can be arbitrarily complex. An important point of note is that, in the general and simplified cases, the expressions are only correct provided the initial assumptions from which they are derived are satisfied, particularly the requirement that there are no sources within the domain depicted in Figure 3. In practice, for typical acquisition geometries in which the recording surface is below the source level, the wavefield separation and redatuming method derived here is applicable between the source and receiver levels. A corollary is that the method is independent of the properties outside the domain of application. In particular, no assumptions about the sea surface — which can be regarded as a secondary source outside the domain of interest — are imposed.

Finally, note that the simplified expressions for wavefield separation in equation 4 are based on the assumption that the recording surface is horizontal. In reality, the streamer profile often deviates from the ideal of a perfectly horizontal streamer. For most practical acquisition geometries of interest, the streamer depth varies smoothly by no more than a few meters over a streamer length of several kilometers such that the streamer can be assumed to be locally horizontal. Nevertheless, whenever necessary, we can revert to the more general form of the wavefield-separation expression given in equation 2 to derive a method for dealing with arbitrary surfaces. Söllner et al. (2008) present such a method and demonstrate its application to field data acquired with an irregular streamer profile.

NOISE CONSIDERATIONS

We have shown that, given perfect recordings of pressure and the component of particle motion normal to the recording surface, it is possible to decompose the wavefield into up- and downgoing parts. In practice, we must also consider the effect of noise sources. A particularly acute issue related to dual-sensor streamers is the effect of mechanical vibrations that are induced as the streamer is towed through the water. Teigen et al. (2012) present a summary of the mechanisms that generate these mechanical vibrations. The noise will be recorded by both pressure and particle motion sensors, but because the amplitude of the particle motion associated with mechanical vibrations is significantly larger than the associated pressure change when measured relative to the seismic signal, the particle motion data are most sensitive to this source of noise. The practical effect is that, for current multicomponent streamers, the overall S/N is improved if the particle motion sensor data are not used for lower frequencies, typically less than 20 Hz (Carlson et al., 2007; Caprioli et al., 2012).

For those frequencies in which it is identified that the noise recorded by the particle motion sensor is excessive, we can emulate the particle motion data using the relatively clean pressure data. This procedure has been described by several authors (e.g., Amundsen, 1993; Fokkema and van den Berg, 1993; Amundsen et al., 1995) and can be derived by evaluating the wavefield-separation equations 4 at the sea surface ($z_o = 0$). If the sea surface can be assumed to behave as a free surface, the total pressure (i.e., the sum of P^{up} and P^{down}) at this surface is zero by definition. Imposing this boundary condition, and assuming a flat streamer, yields the following expression for the vertical component of particle velocity as a function of pressure (e.g., Amundsen et al., 1995):

$$V_z(k_x, k_y, \omega|z_r) = -\frac{k_z}{\omega\rho}\left(\frac{1+\exp(-2ik_z z_r)}{1-\exp(-2ik_z z_r)}\right)P(k_x, k_y, \omega|z_r). \quad (6)$$

Note that, in the case in which the source is shallower than the streamer, the evaluation of the expressions in equation 4 at the sea surface violates the requirement that there are no sources between the recording level and the output level. Consequently, equation 6 is only valid for scattered energy that is affected by the receiver side ghost: The direct arrival has no receiver side ghost and so needs only to be scaled by the factor, $-k_z/\omega\rho$. However, the vertical component of the velocity field for sources above the streamer, with

proper handling of the direct incident wavefield, may be derived from the measured pressure wavefield using the knowledge of the source signatures (Amundsen et al., 1995).

The denominator in equation 6 represents the ideal pressure ghost function, whereas the numerator is the ideal particle motion ghost. Equation 6 can thus be understood as deconvolution of the pressure ghost function followed by convolution with the particle motion ghost function. The presence of the k_z term in the complex exponential indicates that the ghost period depends on the emergent angle. Figure 4 illustrates the combined effect of source and receiver ghosts for a 7-m source depth and a 15-m receiver depth for the pressure and particle motion sensors as a function of frequency and wavenumber. The dependence of the ghost period on emergent angle is reflected in the frequency-wavenumber dependence of the notch locations in Figure 4.

By substituting the expression for the vertical component of particle velocity from equation 6 into the wavefield-separation expressions in equation 4, we obtain the following:

$$P^{\text{up}}(k_x,k_y,\omega|z_o) = \left(\frac{P(k_x,k_y,\omega|z_r)}{1-\exp(-2ik_z z_r)}\right) \exp(-ik_z(z_r-z_o)),$$
$$P^{\text{down}}(k_x,k_y,\omega|z_o) = -\left(\frac{P(k_x,k_y,\omega|z_r)}{1-\exp(-2ik_z z_r)}\right) \exp(-ik_z(z_r+z_o)). \quad (7)$$

These expressions demonstrate that the method for emulating the low-frequency motion sensor signal followed by wavefield separation is exactly equivalent to deghosting the pressure data by deconvolving the ghost function. There is no decomposition of the wavefield into up- and downgoing parts: The up- and downgoing pressure fields obtained using this method are the same total pressure data with a deghosting filter and extrapolators applied. For cases in which the streamer is not horizontal, Riyanti et al. (2008) present a method for deghosting pressure data acquired for an arbitrary recording surface, which is derived from application of the reciprocity theorem that Fokkema and van den Berg (1993) describe and is a generalization of the deghosting expressions in equation 7. Amundsen et al. (1995) derive a similar approach using Green's theorem.

The deghosting method represented by equation 7 relies on more assumptions than the wavefield-separation procedure applied to dual-sensor streamer data at higher frequencies. Specifically, the method requires information about receiver depth and propagation velocity. The robustness of the method to these assumptions will be discussed later in this paper. Furthermore, the method is based on the assumption that the sea surface behaves as a flat sea surface. Tabti et al. (2009) show that this assumption is reasonable over the frequency range for which it is required for dual-sensor streamer processing. The formulation in equation 7 is based on the assumption of a constant propagation velocity between the recording level and the free surface, although the approach can be generalized by starting from more general Green's functions in equation 2 if such information is available. Similarly, if more information about the sea surface shape is available, the flat sea surface assumption could also be relaxed in principle. Such information might be derived from pressure gradient approximations (Robertsson and Kragh, 2002; Amundsen et al., 2005) or by imaging the sea surface from high-frequency data obtained using a dual-sensor streamer (Orji et al., 2010, 2012).

At higher frequencies, where the S/N conditions are such that the wavefield-separation method yields a usable result, it is possible to further enhance the S/N by exploiting the free surface condition. If the expressions for P^{up} and P^{down} in equation 4 are evaluated at the sea surface ($z_o = 0$) then, if the boundary condition that the total pressure is zero is satisfied, it follows that P^{up} and P^{down} have equal and opposite amplitude. Consequently, if one is subtracted from the other, the signal will constructively interfere whereas any noise will be attenuated. This technique has also been applied to ocean bottom data to improve the S/N (e.g., Hatchell et al., 2012) and will henceforth be referred to as the "mirror-sum" method in this paper. Adopting the convention that we require data with the same polarity as the upgoing pressure field, normalizing to give the same amplitude as for equations 4 and 7 and redatuming to a desired output level z_o yields the following expression:

$$P^{\text{up}}_{\text{ms}}(k_x,k_y,\omega|z_o) = \frac{1}{4}\left((1-\exp(2ik_z z_r))P(k_x,k_y,\omega|z_r) - \frac{\omega\rho}{k_z}(1+\exp(2ik_z z_r))V_z(k_x,k_y,\omega|z_r)\right) \exp(-ik_z(z_r-z_o)). \quad (8)$$

The key difference between equations 8 and 4 is that the pressure and particle motion data are multiplied by the complex conjugate of their respective ghost functions, which is equivalent to correlation with their ghost functions in the time domain thereby removing the phase effects of the ghost. Consequently, the expression in equation 8 is the dual-sensor streamer equivalent of the dephase and

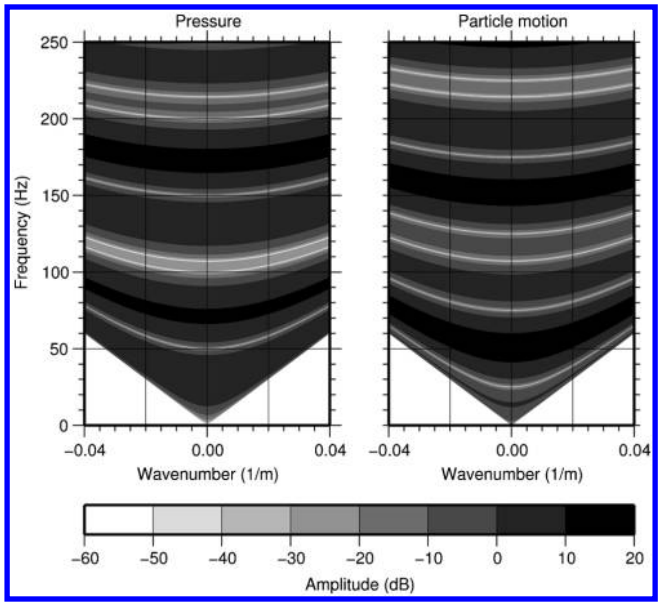

Figure 4. Combined source and receiver ghost functions exhibiting characteristic spectral notches as a function of frequency and horizontal wavenumber for a source at a 7-m depth and a receiver at a 15-m depth for a pressure sensor (left) and a particle motion sensor (right). A water velocity of 1500 m/s is assumed. The common notches at 107 and 214 Hz at zero wavenumber derive from the source.

sum techniques that are commonly applied to deghost over/under streamer data (e.g., Posthumus, 1993). Note that, as for the derivation of the particle velocity as a function of pressure in equation 6, in the case in which the source is located above the receiver level, the expression in equation 8 is not valid for the direct arrival because this event is not affected by the receiver-side ghost.

The schematic in Figure 5 illustrates the noise suppression effect of combining the up- and downgoing wavefields at the free surface compared to straightforward wavefield separation. If there is a source of noise that is recorded by one sensor but not the other, its magnitude is reduced relative to the signal when the data from the two sensors are combined. Examples of such noise sources include strong mechanical vibration noise that is much stronger for the particle motion sensor than the pressure sensor or seismic interference noise from a distant source that is propagating approximately horizontally and is therefore much stronger for the pressure sensor than a vertically oriented particle motion sensor (Cambois et al., 2009b). However, if the up- and downgoing wavefields are recombined after redatuming to the free surface by the method represented by equation 8, the contributions of the two sensors are weighted by their respective ghost functions such that, whenever a particular sensor contributes no signal due to the presence of a spectral notch, its contribution is downweighted to zero. The overall effect is to apply a ghostlike filter to the noise such that it is completely suppressed at frequencies in which there is no signal contribution from the noise-affected sensor and there is no suppression of noise at the frequencies in which that sensor is the sole contributor to the signal. This approach considers only the signal contributions to the output, but a natural extension is to consider the relative noise contributions from each sensor when determining the most appropriate weighting of the contribution of the two sensors (Caprioli et al., 2012). The trade-off is that the free surface condition is imposed, which has consequences for data integrity and robustness.

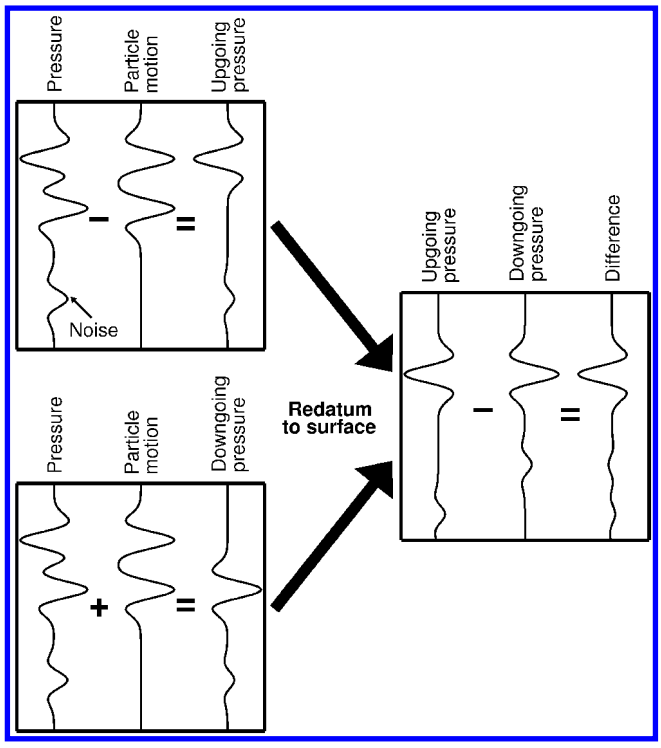

Figure 5. Schematic representation of the mirror sum in the presence of noise recorded by only one of the two sensors (the pressure sensor in this example). The output of all summations has been normalized to maintain consistent primary amplitudes. The combination of the two sensors results in improved S/N compared to the noisy sensor alone, and combining the up- and downgoing wavefields at the free surface further reduces the noise by imposing a ghostlike filter.

ROBUSTNESS ANALYSIS

The various wavefield-separation and deghosting methods that have been presented rely on different assumptions. An important consideration when evaluating the suitability of a particular method is how sensitive it is to errors in those assumptions. For the purposes of this analysis, we suppose that the assumptions that the recording surface is horizontal and the sea surface is a horizontal free surface are correct. The wavefield-separation method represented by equation 4 requires information about propagation velocity and density. The deghosting and mirror-sum methods represented by equations 7 and 8, respectively, also require information about the streamer depth.

We will now consider the effect of errors in density, streamer depth, and propagation velocity for the wavefield-separation, pressure-deghosting, and mirror-sum methods. The accuracy of the obliquity calculation in equation 5 will also be considered. For the wavefield-separation and mirror-sum methods, the effects will be illustrated by showing the amplitude and phase errors introduced at zero offset for a 15-m streamer depth. The effect at shallower and deeper streamer depths can be inferred by stretching or compressing the frequency axis, respectively, such that the notch positions correspond to the alternative depth, and higher emergent angles are equivalent to shallower tow depth at zero offset. In the case of pressure deghosting, an 8-m streamer depth will be considered as a representative acquisition depth for conventional data because this method could, in principle, be used to deghost conventional data.

Finally, to demonstrate the effect of errors on the appearance of dual-sensor streamer data, the time series representations of the output of wavefield separation and mirror sum will be compared to a reference modeled upgoing pressure field for a representative source at a 5-m depth with a recording filter appropriate to a 2-ms sampling interval applied. The results for pressure deghosting of a conventional streamer at an 8-m depth are not shown because this method is not appropriate over the full bandwidth due to the presence of deep spectral notches. For ease of comparison, the source signature corresponding to a vertical take-off angle will be used throughout irrespective of the emergent angle at the receiver. Such events could be generated by a point diffractor located directly beneath the source. Results will be shown with and without the lowest frequencies calculated using pressure deghosting to reflect the procedure that is likely to be applied in practice due to noise considerations. The pressure deghosted and wavefield-separation or mirror-sum results will be merged over a frequency range of 18 to 22 Hz using complementary Hann tapers.

Density errors

Water density information is required as part of the acoustic impedance scaling that is used to match particle velocity and pressure

data. Density can be measured in the field or calculated from measured velocity, depth, and temperature information (Mamaev, 1975; Mackenzie, 1981). Consequently, we can generally expect to have reliable density information available when processing dual-sensor streamer data.

Figure 6 shows the effect of a 5% error in density, which is considered to be at the upper end of the error that is likely to be introduced, at vertical incidence for the three deghosting methods. Density is not required to perform pressure deghosting, so there is no error for this method. For wavefield separation and mirror sum, the amplitude spectrum shows a cyclical error that is maximum every 50 Hz, which corresponds to the notches in the hydrophone spectrum. At these frequencies, the particle motion data are the sole contributors to the signal, so the error due to the density error is maximum. Similarly, at frequencies corresponding to the particle motion sensor notches, only the pressure sensor contributes so there is no error. A very small cyclical phase error is observed for the wavefield-separation result, which is zero at pressure and particle motion sensor notches in which only one of the sensors contributes to the signal, and maximum at frequencies halfway between notches in which the contributions from both sensors are equally weighted and the effect of the scaling discrepancy is largest. This phase error is not present for the mirror-sum method because it is a dephase and sum approach whereby the phase effects of the ghosts for each sensor are removed by correlation with the appropriate ghost function. Figure 7 shows the time series for a typical source. For wavefield separation, there is a small residual error arising from incorrect scaling of the particle motion data resulting in residual downgoing energy and reduced amplitude of the upgoing energy, whereas the residual for the mirror-sum method is the zero-phase equivalent. Overall, Figures 6 and 7 demonstrate that wavefield separation and mirror sum are quite insensitive to errors in the measurement of density of the magnitude that we are likely to encounter in the field.

Depth errors

The streamer depth is usually measured using hydrostatic pressure sensors in the streamer. At any instant in time, the ghost period experienced by a particular receiver will be influenced by the local shape of the sea surface. However, for the purposes of this analysis, we will assume that such effects average out over time and limit the analysis to the effects of persistent systematic errors in streamer depth — although it should be noted that, under rough sea conditions, local errors in the deghosting result could be significantly larger than shown in this section. We will consider the case in which the assumed streamer depth is 0.5 m greater than the true streamer depth. By using properly calibrated depth sensors, streamer depth errors should generally be expected to be less than this. Figure 8 shows the effect of a depth error of 0.5 m for the three deghosting methods. The wavefield-separation method is unaffected by depth errors because the pressure and particle velocity sensors are collocated and experience the effects of the same sea surface, and their ghost responses are always perfectly complementary regardless of depth.

Pressure deghosting exhibits very large amplitude errors such that the method essentially breaks down at about 80% of the first nonzero pressure ghost notch frequency. The phase spectrum exhibits a linearly increasing error, which is related to the difference between the ghost period in the data and the assumed ghost period used in the deghosting operator. However, near the notches there are some frequencies that have incorrect polarity represented by a jump of 180° in the phase spectrum. These jumps occur because the pressure ghost functions have the form of a sine function, easily

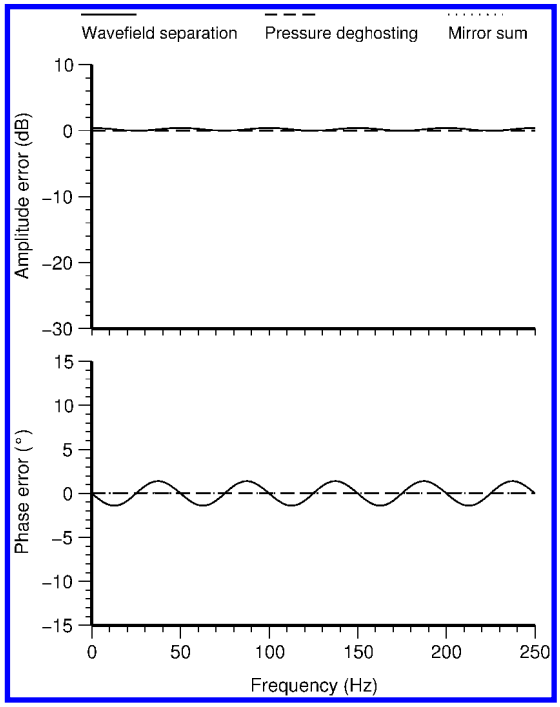

Figure 6. Amplitude and phase errors in the pressure-deghosting, wavefield-separation, and mirror-sum results for a +5% error in the assumed density.

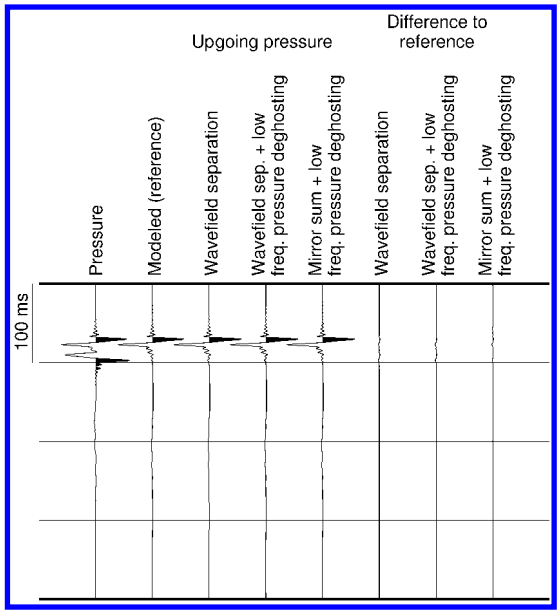

Figure 7. Input pressure data, modeled upgoing-pressure field, and the output obtained from different dual-sensor processing methods in the presence of a +5% error in density. The output of wavefield separation over the full bandwidth, wavefield separation merged with pressure deghosting below ~20 Hz, and mirror sum merged with pressure deghosting are shown, together with the difference to the modeled reference.

seen when expressing the complex exponential by trigonometric functions, with zero crossings at the notches in the amplitude spectrum. Because the zero crossings associated with the ghost in the data occur at different frequencies to those assumed in the deghosting operator, the polarity is incorrect between the true and assumed notch frequencies. These effects limit the utility of this method for deghosting conventionally acquired data: It is known that deghosting pressure data will be unstable near notch locations where the S/N is poor, but Figure 8 demonstrates that the method is highly sensitive to depth errors at significantly lower frequencies. If this method were applied to data acquired at a 15-m depth, as in the dual-sensor streamer case considered in this paper, this instability will occur at lower frequencies because the spectral notches move to lower frequencies as streamer depth increases. Recall that, due to particle motion noise limitations, pressure deghosting is used for the lowest frequencies when processing dual-sensor streamer data. However, because this procedure is generally limited to frequencies of 20 Hz and below, or 40% of the first nonzero notch frequency at a 15-m depth, Figure 8 demonstrates that this method is generally stable over the frequency range for which it is required. This point is further demonstrated in Figure 9, which shows that the use of pressure deghosting below 20 Hz has a negligible effect on the quality of the results even though an incorrect depth has been used.

The mirror-sum method is generally much more stable than pressure deghosting for the small depth error in this example. The same linear phase error as in the pressure-deghosting results is observed, but there is no polarity error associated with the notches. The amplitude spectrum exhibits a slow decay with frequency. This feature can be understood by considering the mirror sum as the subtraction of the downgoing from the upgoing pressure field after redatuming to the sea surface using an incorrect depth. The use of an incorrect depth means there will be a small time shift between the up- and downgoing pressure fields. When evaluated at the streamer depth, the upgoing pressure field will be at the correct time but the downgoing pressure field will be too early. The overall effect is to impose a filter equivalent to an anticausal particle motion ghost with a very small period corresponding to the timing error between the real and assumed ghosts, which has an amplitude spectrum of the form shown for the particle motion sensor in Figure 2. When the depth error is very small, the first spectral notch is at a very high frequency such that, within the bandwidth of interest, the mirror-sum method is relatively insensitive to depth errors.

For all methods, a depth error will also lead to a kinematic error in the redatuming step if the up- and downgoing pressure fields are output at any depth other than the streamer depth. If the assumed streamer depth is larger than the true depth, the upgoing pressure field will be redatumed to a later time than if the true depth were used and the downgoing pressure field will be redatumed to a time that is too early. The magnitude of the timing discrepancy is linearly related to the redatuming distance and the cosine of the emergent angle as illustrated in Figure 10.

Velocity errors

The propagation velocity of sound in water is required to determine the obliquity factor k_z as defined in equation 5. As with density, velocity can be routinely measured in the field to a high degree of precision. For wavefield separation, the velocity at the streamer depth is required to correct for acoustic impedance and obliquity, whereas for pressure deghosting and the mirror-sum method, a measure of the propagation velocity between the streamer depth and the surface is required to accurately determine the ghost period.

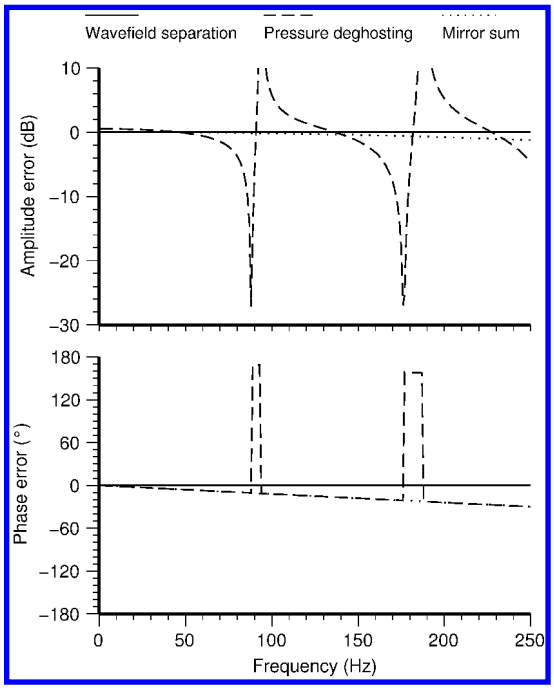

Figure 8. Amplitude and phase errors in the pressure-deghosting, wavefield-separation, and mirror-sum results for a +0.5-m error in the assumed streamer depth.

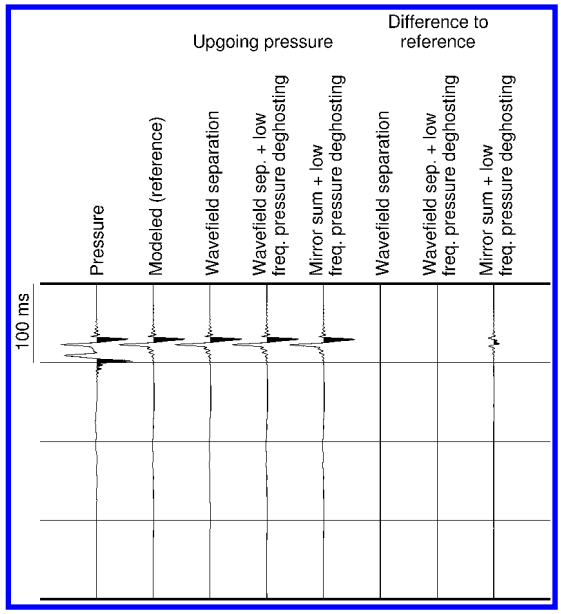

Figure 9. Input pressure data, modeled upgoing pressure field, and the output obtained from different dual-sensor processing methods in the presence of a +0.5-m error in streamer depth. The output of wavefield separation over the full bandwidth, wavefield separation merged with pressure deghosting below ~20 Hz, and mirror sum merged with pressure deghosting are shown, together with the difference to the modeled reference.

At normal incidence ($k_x = k_y = 0$), the expression for k_z reduces to ω/c. In this special case, it is easy to understand the effect of velocity errors on the different deghosting methods. For wavefield separation, a velocity error has the same effect as a density error: A 5% velocity error will have the same effect as a 5% density error, as illustrated in Figure 6. For pressure deghosting, a velocity error has the same effect as a depth error: A velocity estimate that is too high has the same effect as a depth estimate that is too low. The 0.5-m depth error illustrated in Figure 8 is equivalent to a velocity error of −3.3% at a 15-m depth. The kinematic error in the redatuming step will also behave similarly. For the mirror-sum approach, both the preceding effects apply; i.e., a velocity error has the same effect as a density error and a depth error combined.

Away from normal incidence, the qualitative effect of a velocity error is the same, but the magnitude increases compared to the normal incidence case as the magnitude of the horizontal wavenumbers increase. For wavefield separation, this effect can be explained by considering the scaling factor that is applied to the particle-velocity data as the combination of an acoustic impedance term and an obliquity term. Velocity errors affect both of these components; however, although the acoustic impedance term is a constant, the obliquity error is zero at normal incidence but increases in magnitude toward higher emergent angles, represented by higher wavenumbers within a constant frequency slice, leading to increasing sensitivity to velocity errors with increasing emergent angle. For pressure deghosting, higher emergent angles are equivalent to deghosting normal incidence data acquired at a shallower depth, so the increasing sensitivity to velocity errors with emergent angle reflects the increased sensitivity to a given velocity error when the depth is reduced because a given, fixed depth error becomes proportionately larger compared to the true depth.

3D errors

Given the limited crossline sampling for typical 3D acquisition geometries, it is often convenient to process data for each streamer individually. By doing so, we implicitly assume that the crossline horizontal wavenumber (k_y) used in the calculation of the obliquity term k_z in equation 5 is zero. As a result, k_z is systematically overestimated. The effect can thus be considered as comparable to a velocity error.

Figure 11 illustrates the error introduced by the 2D approximation for the case in which energy is assumed to be traveling vertically (i.e., the event appears horizontal in the inline direction), but in fact it has an emergent angle of 30° in the crossline direction, which is ignored. This scenario might occur at the apex of an out-of-plane diffracted event. The obliquity factor k_z is directly proportional to the cosine of the emergent angle. In this case, the cosine of the assumed emergent angle is 1, whereas the cosine of the true emergent angle is 0.866, so the error in k_z arising from the 2D approximation is of the order of 15%, i.e., considerably larger than the errors in density, depth, and velocity hitherto considered. Figure 11 shows that the effect on wavefield separation and pressure deghosting is qualitatively similar to and of greater magnitude than the effects of density and depth errors illustrated in Figures 6 and 8, respectively. The error introduced in the mirror-sum method is a hybrid of the effects of density and depth errors shown in Figure 6 and Figure 8. Because the timing error between the real and assumed ghosts is much larger in the case considered in Figure 11 than for the depth error considered in Figure 8, the ghostlike filter that is imposed has a notch at a much lower frequency such that it lies within the bandwidth shown in Figure 11. This feature is most clearly visible in the phase spectrum, where the phase discontinuity associated with the notch is observed at 187 Hz. The obliquity error also introduces an error in the scaling of the particle motion sensor, which manifests as a sinusoidal amplitude variation superimposed on the longer period amplitude variation due to the ghostlike filter arising from ghost period errors. The phase error is larger than for pressure deghosting of data acquired at an 8-m depth because the

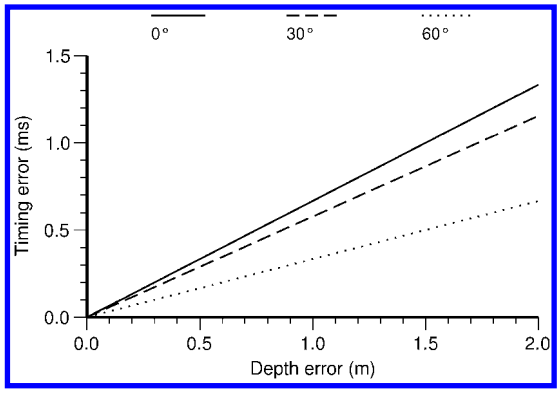

Figure 10. The timing error in the redatuming step as a function of depth error assuming a propagation velocity of 1500 m/s for different emergent angles. Note that the timing error at 60° is half that at normal incidence because the error is related to the cosine of the emergent angle and the cosine of 60° is 0.5.

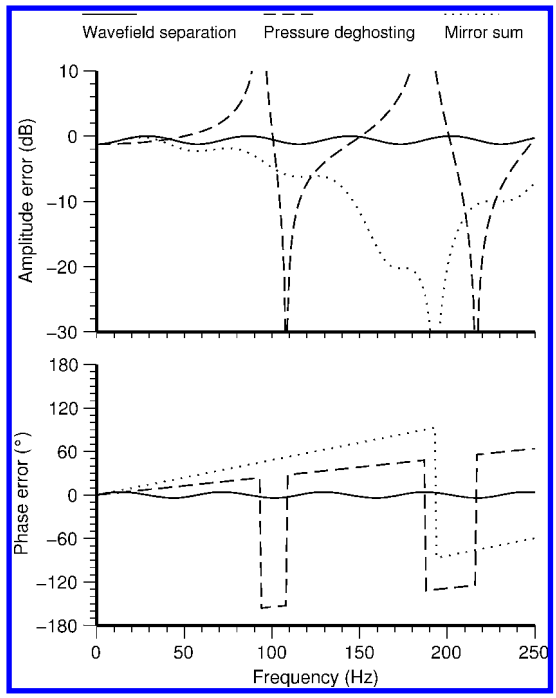

Figure 11. Amplitude and phase errors in the pressure-deghosting, wavefield-separation, and mirror-sum result when an event with an emergent angle of 30° in the crossline direction is processed using a 2D approximation.

effect of a given obliquity error gives an error in the estimate of the ghost period that is proportional to the streamer depth. The time series in Figure 12 further emphasizes that the error in wavefield separation is of similar form, but larger magnitude, to the effect of a 5% density error shown in Figure 7, whereas the mirror-sum method gives a much larger error. Note that the use of pressure deghosting for the lowest frequencies does not significantly degrade the results.

The examples in Figure 11 demonstrate that, for the scenario under consideration, the errors introduced by the 2D approximation can be significant. Of all the methods, the wavefield-separation approach is least susceptible to such errors because the only error that is introduced by the 2D approximation is an error in the scaling of the particle-motion data relative to the pressure data. This will lead to imperfect separation of up- and downgoing energy; i.e., the upgoing pressure field estimate will contain some downgoing energy and vice versa, but overall, the wavefield-separation approach will not break down to the same extent as the other deghosting methods under consideration.

Unlike the other sources of error considered previously, which arise from imperfect measurement of the quantities required to perform wavefield separation, errors due to the 2D approximation are data dependent. Therefore, to understand the effect of the 2D approximation on data quality, it is necessary to evaluate the magnitude of the error that is likely to occur for any particular geologic scenario of interest. The magnitude of the error due to the 2D approximation can be expressed as the ratio of the 2D approximation of obliquity to the true obliquity as follows:

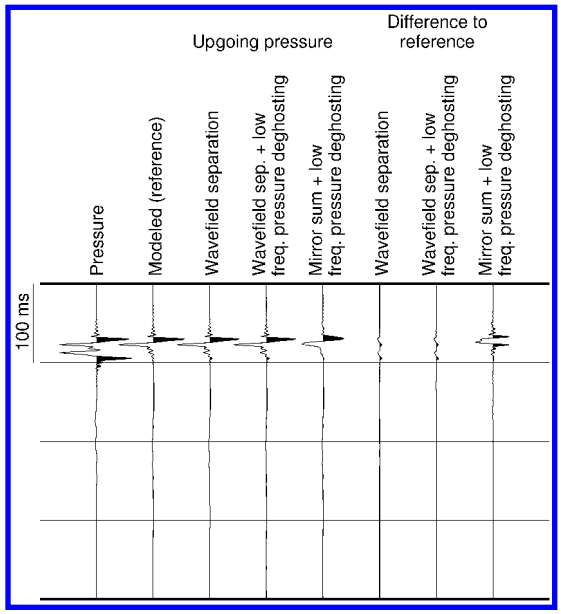

Figure 12. Input pressure data, modeled upgoing pressure field, and the output obtained from different dual-sensor processing methods for an event with an emergent angle of 30° in the crossline direction processed using a 2D approximation. Note that the input total pressure field has a shorter ghost period than the examples in Figures 7 and 9, which were modeled for vertical incidence. The output of wavefield separation over the full bandwidth, wavefield separation merged with pressure deghosting below ~20 Hz, and mirror sum merged with pressure deghosting are shown, together with the difference to the modeled reference.

$$\varepsilon = \sqrt{\frac{\left(\frac{\omega}{c}\right)^2 - k_x^2}{\left(\frac{\omega}{c}\right)^2 - k_x^2 - k_y^2}}. \tag{9}$$

The obliquity error estimate in equation 9 is always greater than or equal to 1: the closer to 1, the more accurate the 2D approximation. For the example in Figures 11 and 12, ε is 1.15. This quantity can be evaluated for a given geologic model using ray tracing to determine the raypath vector for a particular event at the receiver location. Figure 13 shows the value of ε as a function of inline and crossline offset for reflections from horizontal interfaces at selected depths within a representative background velocity model with relatively shallow water (100 m). This figure shows that ε depends only on the crossline offset for the seafloor event (a constant velocity medium). The error for the seafloor reflector for other water depths can easily be inferred from this figure: If the water depth doubles, the crossline offset corresponding to a given error level will also double. The same argument can be used to predict the error for water-column multiples. For all deeper events, the error rapidly decreases with increasing inline offset. Furthermore, there is a general decrease in error with increasing depth. These effects follow from ray-bending effects in media in which velocity increases with depth, so the errors will decay more rapidly for higher velocity gradients. Note that the example in Figure 13 is valid only for horizontal interfaces. However, more complex reflected or diffracted events could be modeled using the same procedure. Figure 13 serves to illustrate that, in general, errors due to the 2D approximation will be largest for shallow events and near offsets, but that the effects are likely to decay rapidly with increasing reflector depth and offset. This assertion is validated by the results of a time-lapse repeatability analysis conducted in the North Sea as Day et al. (2010) describe. Dual-sensor data acquired at a 15-m depth were processed using the 2D approximation to emulate conventional data acquired at an 8-m depth. Day et al. (2010) show that the repeatability is within the expected tolerances at the target level, with a larger residual error only at the seafloor and immediately below that might in part arise from the use of the 2D approximation.

Finally, note that, by using 2D Fourier transforms, we introduce errors in the redatuming step even if the kinematics are correctly represented by the 2D obliquity correction because 2D plane-wave decomposition only handles 2D geometrical spreading, not 3D geometrical spreading as present in the data. This effect can be corrected (e.g., Wapenaar et al., 1992; Amundsen, 1993) but is generally insignificant for all but the shallowest events.

Spatial aliasing

The obliquity calculation in equation 5 is correct only within the unaliased part of the f-k spectrum. For spatially aliased energy, the values of k_x and k_y used to calculate the obliquity factor are systematically too small and errors will result for all methods. Unlike the velocity and 3D errors considered above, the error for spatially aliased energy is frequency dependent. The maximum obliquity errors occur at $2n$ times the Nyquist wavenumber for integer n for both spatial directions because, for these wavenumbers, the wavenumber used in the obliquity calculation is zero. The error introduced increases with increasing emergent angle because spatial

aliasing starts at progressively lower frequencies and the magnitude of the maximum error will also increase.

Figure 14 demonstrates the effects of spatial aliasing for an event with an emergent angle of 60° acquired with spatial sampling of 12.5 m. Such an emergent angle is representative of the upper end of precritical reflected energy commonly recorded, and the spatial sampling under consideration is typical of that commonly available in the inline direction. Figure 14 shows that all methods give perfect results for frequencies below 69 Hz as expected because this is the frequency at which this event is aliased. The error in the wavefield-separation result shows a cyclical pattern with a maximum amplitude deviation of slightly less than 6 dB. This maximum error occurs at frequencies corresponding to notches in the pressure signal spectrum in which only the particle motion sensor contributes to the output, which is thus incorrectly scaled due to the obliquity error. Conversely, at intermediate frequencies, in which only the pressure data contributes, there is no error. The maximum error approaching 6 dB is consistent with the obliquity scaling that should be applied to an event with 60° emergent angle ($\cos 60° = 0.5$) but which is incorrectly calculated in this case. The error for the mirror-sum method exhibits a more complex pattern, including deep notches in which the amplitude is greatly suppressed. The amplitude of the mirror-sum output is always less than or equal to the wavefield-separation output. These notches occur where the correlation of the pressure data and the velocity data with their respective ghost functions yield approximately the same result such that they cancel when combined. Because the two sensors are, in reality, perfectly complementary, this effect can only occur when the ghost functions used in the correlation are grossly in error, as is the case for spatially aliased energy. Overall, these results demonstrate that spatially aliased energy introduces errors for all methods, but these errors are much less severe for the wavefield-separation method than all other methods, which rapidly become completely unstable. This impression is further reinforced by the time-series comparisons in Figure 15.

Spatial aliasing will also introduce a frequency dependent error in the redatuming operator due to the frequency dependent error in the obliquity calculation. Figure 16 illustrates the timing error resulting from redatuming the event considered in Figure 14 through a distance of 10 m. Although there is some frequency dependence, overall, the time shift for the aliased energy approaches twice the correct time shift. This is consistent with the emergent angle of 60° used in this case for which the correct time shift is half the time shift at zero

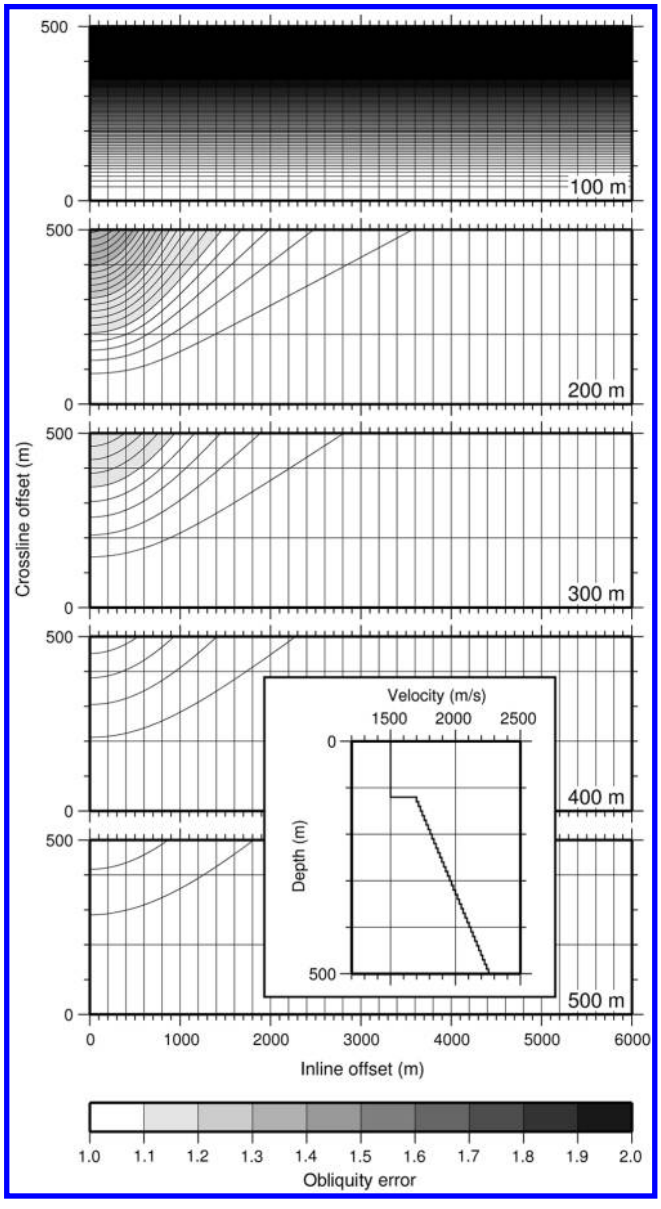

Figure 13. The obliquity error ϵ as defined in equation 9 when the 2D approximation is used to perform the various deghosting operations as a function of inline and crossline offset for several different reflector depths (indicated in the corner of each figure) for a representative velocity model (inset).

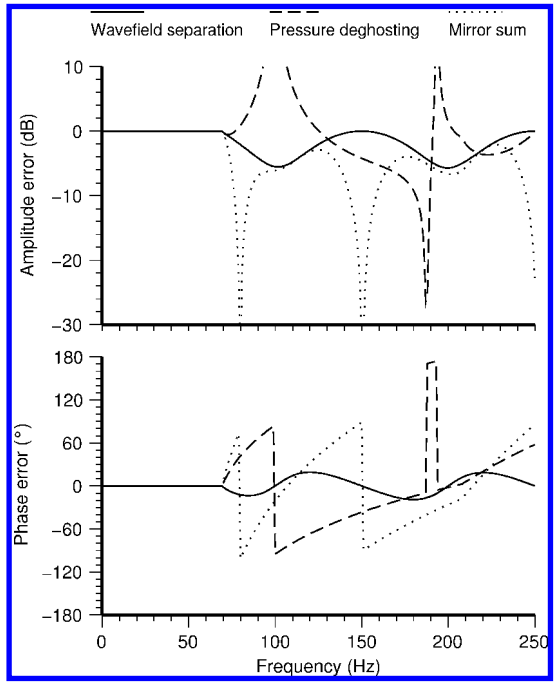

Figure 14. Amplitude and phase errors in the pressure-deghosting, wavefield-separation, and mirror-sum results when an event with an emergent angle of 60° is sampled at a 12.5-m interval and processed without further data interpolation.

offset, and when the obliquity factor is systematically underestimated, the time shift approaches the zero offset result at high frequencies. Note that the absolute error at any given frequency is directly proportional to the redatuming distance.

The errors illustrated in Figures 14 and 16 are representative of a high emergent angle event for spatial sampling typical of the inline direction. In practice, such effects will be mostly confined to shallow data in which the signal bandwidth is widest and the emergent angles largest. However, if the same principles are applied to the crossline direction, where spatial sampling is typically much worse, the effects will be much more severe and will start at much lower frequencies: For 100-m spatial sampling, an event with an emergent angle of 60° will be aliased at 8.5 Hz. Because the error introduced by spatial aliasing shown in Figure 14 is greater than that introduced by the 2D approximation shown in Figure 11, especially if aliasing effects are extended to much lower frequencies due to coarse crossline sampling, these figures show that the 2D approximation will give better results than a 3D method that does not address spatial aliasing.

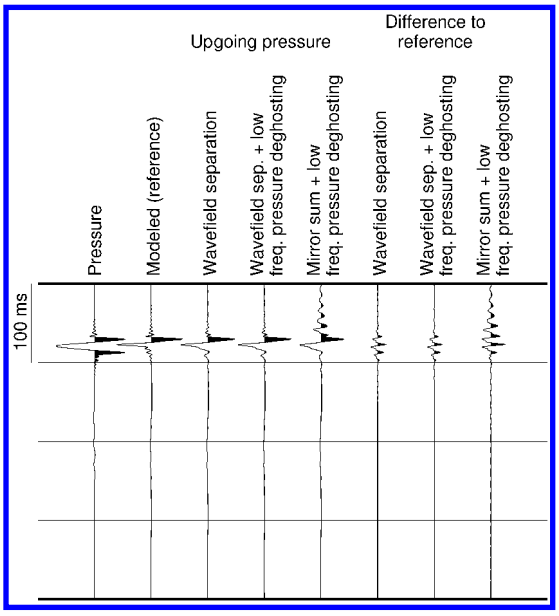

Figure 15. Input pressure data, modeled upgoing pressure field, and the output obtained from different dual-sensor processing methods for an event with an emergent angle of 60° sampled at a 12.5-m interval and processed without further data interpolation. Note that the input total pressure field has a smaller ghost period than the examples in Figures 7, 9, and 12 due to the increase in emergent angle. The output of wavefield separation over the full bandwidth, wavefield separation merged with pressure deghosting below ~20 Hz, and mirror sum merged with pressure deghosting are shown, together with the difference to the modeled reference.

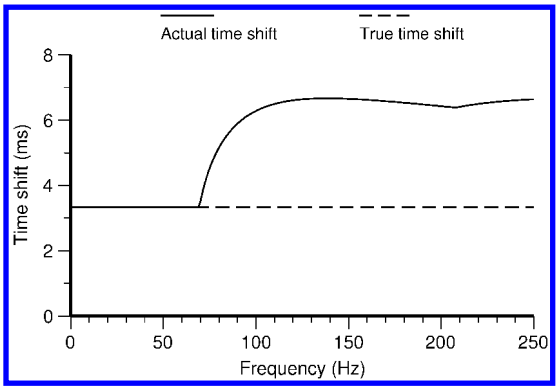

Figure 16. The actual time shift that is applied when data with an emergent angle of 60° sampled at a 12.5-m interval are redatumed through a distance of 10 m as a function of frequency. The true time shift should be invariant with frequency.

PROCESSING METHODS FOR MITIGATING OBLIQUITY ERRORS

We have shown that the largest errors in deghosting are introduced when we use a 2D approximation to process data with significant crossline dips and for spatially aliased energy. Both of these errors arise from incorrect estimation of the vertical wavenumber k_z. It has also been shown that, in general, these errors primarily affect only the shallowest events and are relatively less serious at typical target depths. Nevertheless, it is desirable to find processing solutions for dealing with such issues where they arise.

For typical 3D acquisition geometries, the wavefield sampling in the crossline direction is coarse and comprises very few samples — 10 streamers with 100-m separation is representative. This restriction means that direct application of any of the deghosting methods is not viable due to spatial aliasing, which has been shown to cause instability for all deghosting methods that will be particularly severe for typical streamer spacing, and edge effects due to the restricted aperture (Amundsen, 1993). Wherever it is necessary to process data in a true 3D sense, these limitations must be overcome. Two practical solutions are considered.

The first solution is to use data reconstruction techniques to emulate denser acquisition with increased aperture. Many such data reconstruction techniques have been published (e.g., Liu and Sacchi, 2004; Abma and Kabir, 2006; Schonewille et al., 2009). Recordings of the crossline component of particle motion can also aid this data reconstruction because such data can be used to account for one order of spatial aliasing (Robertsson et al., 2008). After data reconstruction, the data can be transformed into f-k_x-k_y space and processed using the methods previously described. Klüver et al. (2009) demonstrate the application of such a method to structurally complex 3D data acquired with six streamers at a 100-m separation.

The second alternative is to process each cable individually but to use other sources of information to constrain the crossline wavenumber (k_y) that cannot be determined by considering a single streamer in isolation. Klüver and Day (2011) describe an approach whereby the data for each streamer are processed multiple times using 2D plane-wave decomposition for different assumed constant crossline slownesses p_y, such that the obliquity factor in equation 5 is calculated assuming $k_y = \omega\, p_y$. The crossline slowness is then determined for each sample, and the output record is constructed by interpolation between the results for closest modeled slownesses. These crossline slowness estimates could be obtained from the data itself or be determined from a velocity model as described by Fomel (2007). Note that the method of determining the local crossline slowness from a velocity model is correct for primary events only and is only applicable to relatively simple geologic scenarios. For structurally complex data, an approach based on dip scans to obtain the crossline slowness from the data is likely to yield a better result.

Both methods have advantages and disadvantages. The quality of the result from the data reconstruction plus f-k_x-k_y processing is heavily dependent on the quality of the reconstructed traces: Where these data are close to the data that would have been recorded, a near-perfect result can be expected. However, it is very difficult to verify that this has been achieved in practice, and modest errors in the data reconstruction can lead to an inferior result compared to using the 2D approximation. By contrast, the method using local slowness estimates makes use solely of recorded data. Wherever the crossline slowness estimate is close to zero, the result will be identical to that obtained using the 2D approximation, which has been shown to be a reasonable approximation for most of data in most practical scenarios of interest. Furthermore, the use of 2D plane-wave decomposition avoids any errors in the estimation of the vertical wavenumber due to crossline aliasing. However, in its simplest form, the local slowness estimate applies only to the dominant event at a given location; other events will not be handled correctly. In principle, these conflicting events can be handled more easily using the data reconstruction approach provided the data reconstruction recreates all the conflicting events adequately. Note also that the local slowness approach is still based on 2D plane-wave decomposition, so any effects related to geometrical spreading associated with redatuming or ghosts will only be accounted for in a 2D rather than a 3D sense, unlike when processing is carried out in f-k_x-k_y space. In practice, these effects are mostly confined to the very shallowest events and can, in principle, be corrected by other means.

Figure 17 demonstrates the improvement in the accuracy of the processing when the crossline slowness is taken into account for a field-data example acquired in shallow water with 275-m crossline offset, for which the errors from the 2D approximation can be expected to be significant. This figure shows the sum of the up- and downgoing pressure after redatuming to the surface for a single near-offset channel, which should ideally be zero if the sea surface behaves approximately as a flat sea surface. In practice, this ideal will never be fully achieved, but Figure 17 shows that the residual energy for the shallowest reflectors is significantly reduced when local slowness estimates based on the velocity structure are used. The spectral comparison indicates that there is no residual energy below 20 Hz because data below this frequency are derived solely from the pressure data using a flat free-surface assumption; hence, it is a mathematical certainty that the sum of the up- and downgoing pressure at the surface will be zero because this boundary condition has already been imposed. There is a significant reduction in residual energy between 20 and 100 Hz when the crossline slowness information is used, which indicates a physically more correct processing result. Above 100 Hz, the residual energy in both cases is similar to the energy in the upgoing pressure field. This effect is thought to be due to incorrect treatment of energy aliased in the inline direction because the most energetic events in the analysis window have a significant emergent angle, and the inline spatial sampling for these data is 12.5 m. Finally, note that there is hardly any residual energy at traveltimes more than 400 ms below the seafloor even when we do not take account of the local crossline slowness, which demonstrates that the errors due to the 2D approximation of the vertical wavenumber are almost entirely confined to the shallowest events.

Data reconstruction is a more viable option for dealing with errors in the vertical wavenumber estimation due to spatial aliasing in the inline direction because there are usually many more samples that are more closely spaced compared to the crossline direction. In the case in which all sources are at one end of the streamers, a further approach that can be adopted is to apply a linear moveout to the data. Processing may then be carried out using a vertical wavenumber calculated as follows:

$$k_z = \sqrt{\left(\frac{\omega}{c}\right)^2 - \left(k_x + \frac{\omega}{v_{\mathrm{LMO}}}\right)^2 - k_y^2}, \qquad (10)$$

where v_{LMO} is the apparent inline velocity used in the linear moveout application. When compared to the case in which no linear moveout is applied, a positive linear moveout velocity will give a more accurate result for positive wavenumbers and a less accurate result for negative wavenumbers, which will give a more accurate result overall if most of the signal maps to positive wavenumbers. For example, for data acquired with 12.5-m spatial sampling, the application of a linear moveout with $v_{\mathrm{LMO}} = 3000$ m/s allows all forward-scattered energy to be processed accurately up to 120 Hz, which is sufficient for data with 4-ms temporal sampling. The linear moveout method can be combined with data reconstruction depending on the spatial and temporal sampling of the input data and the required bandwidth.

Figure 18 demonstrates the application of the linear moveout technique to improve the accuracy of the wavefield separation to a field data example from the same experiment as in Figure 17. In Figure 18, a single channel with an inline offset of 1584 m

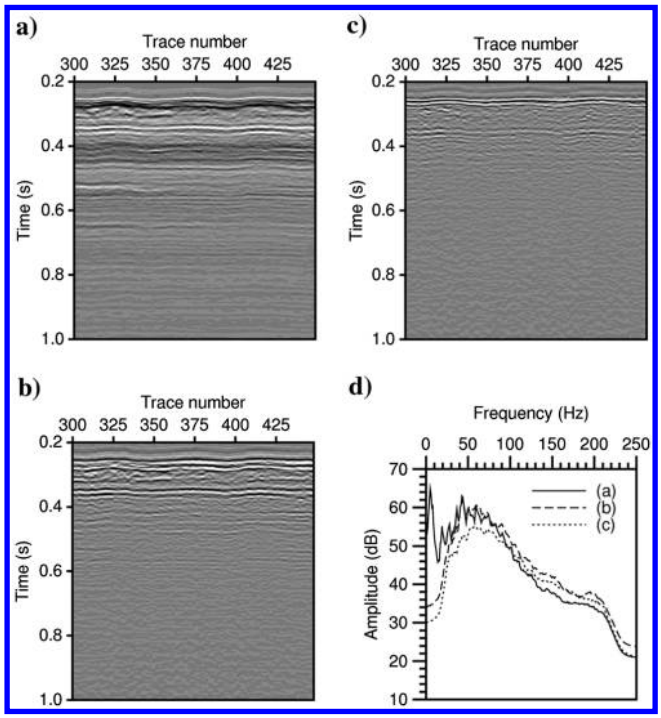

Figure 17. Example field data acquired in shallow water. A single channel with a nominal inline offset of 196 m and a nominal crossline offset of 275 m is shown. (a) Upgoing pressure field at recording depth. (b) Sum of the up- and downgoing pressure fields after redatuming to the sea surface. (c) Sum of the up- and downgoing pressure fields after redatuming to the sea surface with a local correction for the crossline slowness derived from a velocity model. (d) Amplitude spectra for all three cases for a window from 0.3 to 1.0 s.

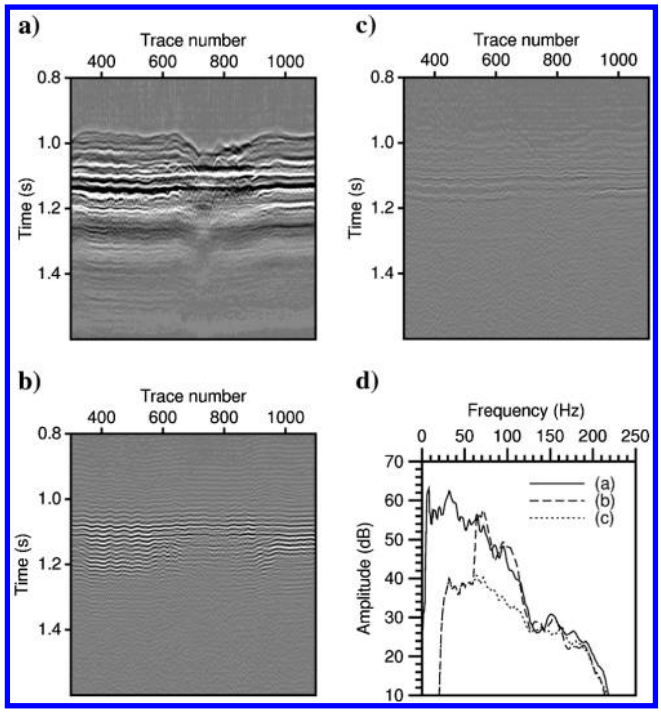

Figure 18. Example field data acquired in shallow water. A single channel with a nominal inline offset of 1584 m and a nominal crossline offset of 75 m is shown. (a) Upgoing pressure field at recording depth. (b) Sum of the up- and downgoing pressure fields after redatuming to the sea surface. (c) Sum of the up- and downgoing pressure fields after redatuming to the sea surface with a linear moveout applied to better treat spatially aliased energy. (d) Amplitude spectra for all three cases for a window from 0.8 to 1.6 s.

and crossline offset of 75 m is used. The residual energy compared to the upgoing pressure energy is much smaller than in Figure 17 even though the 2D approximation has been used because the crossline offset is much smaller. Nevertheless, significant residual energy is observed, which is substantially reduced when a linear moveout is applied. The spectral comparison shows that the reduction in residual energy is confined to frequencies in excess of 60 Hz, which is consistent with more correct treatment of spatially aliased energy for data acquired with 12.5-m spatial sampling.

CONCLUSIONS

A dual-sensor streamer records the pressure and vertical component of particle velocity using collocated sensors. The sea-surface ghosts recorded by these two sensors are perfectly complementary such that, at frequencies in which one sensor has a spectral notch due to perfect destructive interference between the upgoing scattered energy and its ghost, the other sensor experiences perfect constructive interference. As a result, when the data from the two sensors are combined, the S/N is usable at a wider range of frequencies than if either sensor is considered in isolation.

It is well known that, given recordings of the pressure and particle velocity normal to the recording surface, it is possible to separate the wavefield into up- and downgoing parts, which is a useful process for exploiting the extended bandwidth. Data acquired using streamers containing only pressure sensors can be deghosted by deconvolving the ghost function, but this procedure is only applicable away from spectral notch frequencies. In real field acquisition scenarios, we also have to consider the effect of noise sources. In particular, noise arising from mechanical vibrations as the streamer is towed through the water is particularly significant for the particle motion sensor such that a better overall result is obtained if these data are discarded for frequencies below 20 Hz. At higher frequencies, S/N can be further improved by recombining the up- and downgoing pressure fields after redatuming to the free surface — the mirror-sum approach. When this procedure is applied, a ghostlike filter is applied to the noise thereby reducing its amplitude at certain frequencies.

The robustness of the various deghosting methods to errors in the parameters that each of them requires was investigated. Wavefield-separation and the mirror-sum methods applied to dual-sensor data were compared to deghosting conventional streamer data acquired at a typical depth. Density information is required to correctly scale the particle motion data relative to the pressure data, and the density uncertainties that we are likely to encounter were shown to have a very small impact on the quality of the result. All methods apart from wavefield separation require streamer depth information. The mirror-sum method was shown to be relatively insensitive to typical streamer-depth uncertainties, whereas deghosting conventional data was shown to introduce significant instability even at frequencies away from the spectral notches. Errors in the propagation velocity have the same effect as small density and depth errors combined. Whenever the estimation of the vertical wavenumber is in error, either because we have chosen to ignore the crossline component of propagation or due to incorrect treatment of aliased energy, errors can be introduced that are much more significant than those introduced by density, depth, or velocity errors. For the examples considered in this paper, the wavefield-separation method continues to give a reasonable result, whereas the other methods break down completely.

It should be noted that the effects of vertical wavenumber errors will primarily affect the shallowest reflectors only and are usually negligible at typical target depths of interest. Nevertheless, it is useful to consider processing approaches that can be adopted to mitigate the effects of such errors in cases in which they are significant. Two such approaches were described. Because spatial aliasing is particularly severe in the crossline direction for typical 3D acquisition geometries, it is advantageous to process each streamer independently, but by doing so we neglect the crossline component of propagation. If an independent measure of the local crossline slowness is available, for example, from a velocity model or dip-scan, a local correction for crossline propagation can be applied. Spatial aliasing can be overcome by interpolation to a finer spatial sampling prior to wavefield separation, which is an appropriate technique provided the sampling is sufficient. In cases in which the energy can be presumed to arrive dominantly from one end of the streamer, application of an inline linear moveout in conjunction with a modified vertical-wavenumber calculation can be beneficial. The effect of these methods was demonstrated using field-data examples and shown to give a physically more correct wavefield-separation result.

ACKNOWLEDGMENTS

We thank the crew of the PGS Atlantic Explorer who acquired the field data shown in this paper and PGS for permission to publish this paper.

REFERENCES

Abma, R., and N. Kabir, 2006, 3D interpolation of irregular data with a POCS algorithm: Geophysics, **71**, no. 6, E91–E97, doi: 10.1190/1.2356088.

Amundsen, L., 1993, Wavenumber-based filtering of marine point source data: Geophysics, **58**, 1335–1348, doi: 10.1190/1.1443516.

Amundsen, L., B. Arntsen, A. Reitan, E. Ø. Dischler, and B. Ursin, 2008, Wave equation depth migration — A new method of solution: 78th Annual International Meeting, SEG, Expanded Abstracts, 2252–2256.

Amundsen, L., T. Røsten, J. O. A. Robertsson, and E. Kragh, 2005, Rough-sea deghosting of streamer seismic data using pressure gradient approximations: Geophysics, **70**, no. 1, V1–V9, doi: 10.1190/1.1852892.

Amundsen, L., B. G. Secrest, and B. Arntsen, 1995, Extraction of the normal component of the particle velocity from marine pressure data: Geophysics, **60**, 212–222, doi: 10.1190/1.1443749.

Backus, M. M., P. E. Murray, R. J. Graebner, and R. A. Hardage, 2007, OBC sensor response and calibrated reflectivity: 77th Annual International Meeting, SEG, Expanded Abstracts, 1044–1048.

Barr, F. J., and J. I. Sanders, 1989, Attenuation of water-column reverberations using pressure and velocity detectors in water-bottom cable: 59th Annual International Meeting, SEG, Expanded Abstracts, 653–656.

Bunting, T., B. J. Lim, Ch. H. Lim, E. Kragh, G. Rongtao, S. K. Yang, Z. B. Zhang, Y. H. Xie, and L. Li, 2011, Marine broadband case study offshore China: First Break, **29**, 67–74.

Cambois, G., D. Carlson, C. Jones, M. Lesnes, W. Söllner, and H. Tabti, 2009b, Dual-sensor streamer data: Calibration, acquisition QC and attenuation of seismic interferences and other noises: 79th Annual International Meeting, SEG, Expanded Abstracts, 142–146.

Cambois, G., A. Long, G. Parkes, T. Lundsten, A. Mattsson, and E. Fromyr, 2009a, Multi-level airgun array: A simple and effective way to enhance the low frequency content of marine seismic data: 79th Annual International Meeting, SEG, Expanded Abstracts, 152–156.

Caprioli, P. B. A., A. K. Özdemir, A. Özbek, J. E. Kragh, D. J. van Manen, P. A. F. Christie, and J. O. A. Robertsson, 2012, Combination of multicomponent streamer pressure and vertical particle velocity — Theory and application to data: 74th Annual International Conference and Exhibition, EAGE, Extended Abstracts, A033.

Carlson, D., A. Long, W. Söllner, H. Tabti, R. Tenghamn, and N. Lunde, 2007, Increased resolution and penetration from a towed dual-sensor streamer: First Break, **25**, 71–77.

Claerbout, J. F., 1976, Fundamentals of geophysical data processing: Blackwell Scientific Publications.

Day, A., M. Widmaier, T. Høy, and B. Osnes, 2010, Time-lapse acquisition with a dual-sensor streamer over a conventional baseline survey: First Break, **28**, 79–87.

Egan, M., K. G. El-Kasseh, and N. Moldoveanu, 2007, Full deghosting of OBC data with over/under source acquisition: 77th Annual International Meeting, SEG, Expanded Abstracts, 31–35.

Fokkema, J. T., and P. M. van den Berg, 1993, Seismic applications of acoustic reciprocity: Elsevier Science Publishing.

Fomel, S., 2007, Velocity-independent time-domain seismic imaging using local event slopes: Geophysics, **72**, no. 6, U89–U94, doi: 10.1190/1.2781533.

Frijlink, M., R. van Borselen, and W. Söllner, 2011, The free surface assumption for marine data-driven demultiple methods: Geophysical Prospecting, **59**, 269–278, doi: 10.1111/j.1365-2478.2010.00914.x.

Ghosh, S. K., 2000, Deconvolving the ghost effect of the water surface in marine seismics: Geophysics, **65**, 1831–1836, doi: 10.1190/1.1444866.

Hatchell, P. J., M. Tatanova, and A. C. Evans, 2012, Suppressing 4D-noise by weighted stacking of up-going and down-going wave-fields: 74th Annual International Conference and Exhibition, EAGE, Extended Abstracts, E011.

Hill, D., C. Combee, and J. Bacon, 2006, Over/under acquisition and data processing: The next quantum leap in seismic technology?: First Break, **24**, 81–95.

Ikelle, L. T., and L. Amundsen, 2005, Introduction to petroleum seismology: SEG Investigations in Geophysics Series 12.

Klüver, T., 2009, Wavefield separation of dual-sensor towed streamer data using Kirchhoff type datuming and migration operators: 79th Annual International Meeting, SEG, Expanded Abstracts, 2944–2948.

Klüver, T., P. Aaron, D. Carlson, A. Day, and R. van Borselen, 2009, A robust strategy for processing 3D dual-sensor towed streamer data: 79th Annual International Meeting, SEG, Expanded Abstracts, 3088–3092.

Klüver, T., and A. Day, 2011, Processing 3-D dual-sensor towed streamer data using local crossline slowness estimates: 81st Annual International Meeting, SEG, Expanded Abstracts, 3556–3560.

Lameloise, C., W. Söllner, S. Hegna, and N. D. Whitmore, 2012, Broadband depth imaging from separated wavefields: 74th Annual International Conference and Exhibition, EAGE, Extended Abstracts, X047.

Liu, B., and M. D. Sacchi, 2004, Minimum weighted norm interpolation of seismic records: Geophysics, **69**, 1560–1568, doi: 10.1190/1.1836829.

Loewenthal, D., 1994, On dual field measurements using geohydrophones: 64th Annual International Meeting, SEG, Expanded Abstracts, 861–864.

Mackenzie, K. V., 1981, Nine-term equation for the sound speed in oceans: Journal of the Acoustical Society of America, **70**, 807–812, doi: 10.1121/1.386920.

Mamayev, O. I., 1975, Temperature-salinity analysis of world ocean waters: Elsevier Scientific Publishing, Elsevier Oceanography Series 11.

Moldoveanu, N., L. Combee, M. Egan, G. Hampson, L. Sydora, and W. Abriel, 2007, Over/under towed-streamer acquisition: A method to extend seismic bandwidth to both higher and lower frequencies: The Leading Edge, **26**, 41–58, doi: 10.1190/1.2431831.

Orji, O., W. Söllner, and L. J. Gelius, 2010, Imaging the sea surface using a dual-sensor towed streamer: Geophysics, **75**, no. 6, V111–V118, doi: 10.1190/1.3496439.

Orji, O. C., W. Söllner, and L. J. Gelius, 2012, Effects of time-varying sea surface in marine seismic data: Geophysics, **77**, no. 3, P33–P43, doi: 10.1190/geo2011-0361.1.

Özbek, A., M. Vassallo, K. Özdemir, D.-J. van Manen, and K. Eggenberger, 2010, Crossline wavefield reconstruction from multicomponent streamer data: Part 2 — Joint interpolation and 3D up/down separation by generalized matching pursuit: Geophysics, **75**, no. 6, WB69–WB85, doi: 10.1190/1.3497316.

Özdemir, K., A. Özbek, D-J. van Manen, and M. Vassallo, 2010, On data-independent multicomponent interpolators and the use of priors for optimal reconstruction and 3D up/down separation of pressure wavefields: Geophysics, **75**, no. 6, WB39–WB51, doi: 10.1190/1.3494621.

Parkes, G., and S. Hegna, 2011, An acquisition system that extracts the earth response from seismic data: First Break, **29**, 81–87.

Posthumus, B. J., 1993, Deghosting using a twin streamer configuration: Geophysical Prospecting, **41**, 267–286, doi: 10.1111/j.1365-2478.1993.tb00570.x.

Riyanti, C. D., R. G. van Borselen, P. M. van den Berg, and J. T. Fokkema, 2008, Pressure wave-field deghosting for non-horizontal streamers: 78th Annual International Meeting, SEG, Expanded Abstracts, 2652–2656.

Robertsson, J., and E. Kragh, 2002, Rough-sea deghosting using a single streamer and a pressure gradient approximation: Geophysics, **67**, 2005–2011, doi: 10.1190/1.1527100.

Robertsson, J. O. A., I. Moore, M. Vassallo, K. Özdemir, D.-J. van Manen, and A. Özbek, 2008, On the use of multicomponent streamer recordings for reconstruction of pressure wavefields in the crossline direction: Geophysics, **73**, no. 5, A45–A49, doi: 10.1190/1.2953338.

Schneider, W. A., and M. M. Backus, 1964, Ocean-bottom seismic measurements off the California Coast: Journal of Geophysical Research, **69**, 1135–1143, doi: 10.1029/JZ069i006p01135.

Schonewille, M., A. Klaedtke, and A. Vigner, 2009, Anti-alias anti-leakage Fourier transform: 79th Annual International Meeting, SEG, Expanded Abstracts, 3249–3253.

Söllner, W., A. Day, and H. Tabti, 2008, Space-frequency domain processing of irregular dual-sensor towed streamer data: 78th Annual International Meeting, SEG, Expanded Abstracts, 1078–1082.

Sønneland, L., L. E. Berg, P. Eidsvig, A. Haugen, B. Fotland, and J. Vestby, 1986, 2-D deghosting using vertical receiver arrays: 56th Annual International Meeting, SEG, Expanded Abstracts, 516–519.

Soubaras, R., and R. Dowle, 2010, Variable-depth streamer — A broadband marine solution: First Break, **28**, 89–96.

Tabti, H., A. Day, T. Schade, M. Lesnes, and T. Høy, 2009, Conventional versus dual-sensor streamer data de-ghosting: A case study from a Haltenbanken survey: First Break, **27**, 101–108.

Teigen, O., K. Ozdemir, B. A. Kjellesvig, N. Goujon, and J. Pabon, 2012, Characterization of noise modes in multicomponent (4C) towed-streamer: 74th Annual International Conference and Exhibition, EAGE, Extended Abstracts, Z013.

Tenghamn, R., S. Vaage, and C. Borresen, 2007, A dual-sensor towed marine streamer: Its viable implementation and initial results: 77th Annual International Meeting, SEG, Expanded Abstracts, 989–993.

van Borselen, R., R. Hegge, T. Martin, S. Barnes, and P. Aaron, 2011, Enhanced demultiple by 3D SRME using dual-sensor measurements: The Leading Edge, **30**, 920–926, doi: 10.1190/1.3626500.

Vasconcelos, I., 2011, Source-receiver reverse-time imaging of vector-acoustic seismic data: 81st Annual International Meeting, SEG, Expanded Abstracts, 3184–3189.

Vassallo, M., A. Özbek, K. Özdemir, and K. Eggenberger, 2010, Crossline wavefield reconstruction from multicomponent streamer data: Part 1 — Multichannel interpolation by matching pursuit (MIMAP) using pressure and its crossline gradient: Geophysics, **75**, no. 6, WB53–WB67, doi: 10.1190/1.3496958.

Wapenaar, C. P. A., D. J. Verschuur, and P. Herrmann, 1992, Amplitude preprocessing of single- and multicomponent seismic data: Geophysics, **57**, 1178–1188, doi: 10.1190/1.1443331.

Weglein, A. B., and B. G. Secrest, 1990, Wavelet estimation for a multidimensional acoustic or elastic earth: Geophysics, **55**, 902–913, doi: 10.1190/1.1442905.

Whitmore, N. D., A. A. Valenciano, and W. Söllner, 2010, Imaging of primaries and multiples using a dual-sensor towed streamer: 80th Annual International Meeting, SEG, Expanded Abstracts, 3187–3192.

Ziolkowski, A. M., 1971, Design of a marine seismic reflection profiling system using air guns as sound source: Geophysical Journal of the Royal Astronomical Society, **23**, 499–530, doi: 10.1111/j.1365-246X.1971.tb01840.x.

This article has been cited by:

1. Niels Grobbe, Joost van der Neut, Evert Slob, Kees Wapenaar, Carlos Almagro Vidal, Guy Drijkoningen. 2015. Unified multi-depth-level field decomposition. *Geophysical Prospecting* n/a-n/a. [CrossRef]
2. Kjetil E. Haavik, Martin Landrø. 2015. Variable source depth acquisition for improved marine broadband seismic data. *GEOPHYSICS* **80**:3, A69-A73. [Abstract] [Full Text] [PDF] [PDF w/Links]
3. Joost van der Neut, Dmitri Alexandrov, Andrey Bakulin. 2015. Shallow virtual source redatuming by multi-dimensional deconvolution. *Geophysical Prospecting* n/a-n/a. [CrossRef]
4. Lasse Amundsen, Johan O. A. Robertsson. 2014. Wave equation processing using finite-difference propagators, Part 1: Wavefield dissection and imaging of marine multicomponent seismic data. *GEOPHYSICS* **79**:6, T287-T300. [Abstract] [Full Text] [PDF] [PDF w/Links]
5. Johan O. A. Robertsson, Lasse Amundsen. 2014. Wave equation processing using finite-difference propagators, Part 2: Deghosting of marine hydrophone seismic data. *GEOPHYSICS* **79**:6, T301-T312. [Abstract] [Full Text] [PDF] [PDF w/Links]
6. Alba Ordoñez, Walter Söllner, Tilman Klüver, Leiv J. Gelius. 2014. Migration of primaries and multiples using an imaging condition for amplitude-normalized separated wavefields. *GEOPHYSICS* **79**:5, S217-S230. [Abstract] [Full Text] [PDF] [PDF w/Links]
7. Charlotte Sanchis, Thomas Elboth*Multicomponent streamer noise characteristics and denoising 4183-4187. [Abstract] [References] [PDF] [PDF w/Links] [Supplemental Material]
8. Yousif I. Kamil, Nizare El Yadari, Massimiliano VassalloBayesian deghosting approach for multimeasurement streamer data 4233-4237. [Abstract] [References] [PDF] [PDF w/Links]
9. Lasse Amundsen*, Harald Westerdahl, Johan O. A. Robertsson, Marlies VasmelPrediction of wavefields by injecting multicomponent seismic measurements into modeling 1842-1847. [Abstract] [References] [PDF] [PDF w/Links] [Supplemental Material]
10. Lasse Amundsen, Hongbo Zhou, Arne Reitan, Arthur B. Weglein. 2013. On seismic deghosting by spatial deconvolution. *GEOPHYSICS* **78**:6, V267-V271. [Abstract] [Full Text] [PDF] [PDF w/Links]
11. Okwudili C. Orji, Walter Sollner, Leiv J. GeliusSea Surface Reflection Coefficient Estimation 51-55. [Abstract] [References] [PDF] [PDF w/Links]